

Article

An Experimental Investigation into the Thermal Characteristics of Bump Foil Journal Bearings

Yu Zhou ¹, Longtao Shao ², Shuai Zhao ¹, Kun Zhu ³, Shuiting Ding ^{1,4}, Farong Du ¹ and Zheng Xu ^{5,*}

¹ Research Institute of Aero-Engine, Aircraft/Engine Integrated System Safety Beijing Key Laboratory, Beihang University, Beijing 100191, China; zybuua@hotmail.com (Y.Z.); zhaoshuai@buaa.edu.cn (S.Z.); dst@buaa.edu.cn (S.D.); dufrong@hotmail.com (F.D.)

² School of Energy and Power Engineering, Beihang University, Beijing 100191, China; sltwhut@163.com

³ Aero Engine Academy of China, Aero Engine Corporation of China, Beijing 100191, China; zkjason1213@163.com

⁴ Department of Aviation Engineering, Civil Aviation University of China, Tianjin 300300, China

⁵ Laboratory of Aeroengine Power System, Beihang Hangzhou Innovation Institute Yuhang, Hangzhou 310023, China

* Correspondence: zheng.xu@buaa.edu.cn

Abstract: Bump foil journal bearings (BFJBs) are widely used in the superchargers of aviation piston engines (APEs). This paper proposes a method to evaluate the operating state of superchargers by monitoring the bearing temperature. A numerical model with a repeating symmetrical structure in the axial direction is established based on a certain type of supercharger, which solves the temperature field of BFJBs with the non-isothermal Reynolds equation and energy equation. It can be used to analyze the effect of thermal expansion on lift-off speed and stop-contact speed. A new test rig and six various BFJBs were designed to check the temperature characteristics of the BFJBs with variable load and speed. By comparing the numerical results with the experimental results, it was shown that the air film temperature increased almost linearly with the increase in bearing load and speed. However, the temperature increase caused by the rotation speed was significantly greater than the load. The structural parameters of the BFJB affected the bearing support stiffness, which had a nonlinear effect on the lift-off speed and air film temperature. Therefore, the proposed method to evaluate the state of superchargers with BFJBs was effective. These thermal characteristics can be used to guide BFJB design and predict the life cycle of BFJBs.

Keywords: bump foil journal bearing (BFJB); thermal characteristics; energy equation; test bench; lift-off speed; numeral calculations; experimental investigation; supercharger



Citation: Zhou, Y.; Shao, L.; Zhao, S.; Zhu, K.; Ding, S.; Du, F.; Xu, Z. An Experimental Investigation into the Thermal Characteristics of Bump Foil Journal Bearings. *Symmetry* **2022**, *14*, 878. <https://doi.org/10.3390/sym14050878>

Academic Editor: Jan Awrejcewicz

Received: 18 March 2022

Accepted: 19 April 2022

Published: 25 April 2022

Publisher's Note: MDPI stays neutral with regard to jurisdictional claims in published maps and institutional affiliations.



Copyright: © 2022 by the authors. Licensee MDPI, Basel, Switzerland. This article is an open access article distributed under the terms and conditions of the Creative Commons Attribution (CC BY) license (<https://creativecommons.org/licenses/by/4.0/>).

1. Introduction

Bump foil journal bearings (BFJB) are compliant, self-acting hydrodynamic air bearings, with a thin hydrodynamic air film between the rotor and the top foil. The bump foil elastic support structure of BFJBs is a repeating symmetrical structure in the axial direction [1]. Compared with oil-lubricated bearings, BFJBs have distinct advantages of power density, which is conducive to improving the power-to-weight ratio of aviation piston engines (APEs). Some studies have shown that BFJBs can reduce the weight of small aviation engines by 15% and improve reliability by 10 times [2–4]. Moreover, BFJBs have the distinct advantages of low friction loss, long average life, high precision, and high efficiency, in addition to requiring no lubrication [5]. The hydrodynamic lubrication method can avoid the failure of superchargers caused by oil leakages and overcome extremely low-temperature environments at high altitudes [6,7], resulting in substantial benefits to the aerospace community.

With improvements to the flight envelope of APEs, the requirements for superchargers are also increasing [8,9]. BFJBs are selected for the turbocharger rotor system of APEs due to

their high-speed stability and reliability [10,11]. The main parameters for evaluating BFJBs include lift-off speed, friction torque, and temperature characteristics, which significantly affect the performance of BFJBs. Although some parameters of BFJBs can be solved by numerical calculations, it is impossible to accurately calculate their parameters in real operating conditions due to simplifying assumptions. The programming and debugging processes of these algorithms are very complicated, and not suitable for engineering applications [12].

The performance of BFJBs is usually measured indirectly by experiments, which are costly [13–15]. If the working state of the bearing can be quickly evaluated directly through some parameters, the reliability of the bearing can be monitored and the life of the bearing can be predicted [16,17]. Since it is difficult to directly monitor the lift-off time and frictional resistance torque of BFJBs in practical applications, it is almost impossible to evaluate the operating status of BFJBs in real time. The method of directly measuring the temperature of BFJBs is practical and effective, and proper temperature management is beneficial to improving the capacity of bearings at high speed [18].

Many analytical and experimental investigations have been implemented to explore the thermal characteristics of BFJBs. NASA and the U.S. Air Force have developed multi-blade models that have been successfully used in military and commercial aircraft such as the Boeing 767, Boeing 757, and DC-10 gas foil bearings (GFBs) [19,20]. DellaCorte et al. established a high-temperature test bench for GFBs to measure the bearing capacity under high temperature and speed conditions, and concluded that the bearing capacity decreased with the increase in temperature [21]. Braun built a thrust foil air bearing test bench with a maximum test speed of 80,000 r/min, which was used by NASA to develop a future non-lubricated turbine engine [22]. The team of Feng K, from Hunan University, designed and built a GFB to measure the bearing temperature characteristics and rotor dynamic response under different rotational speed and load conditions, and successfully applied it to oil-free turbochargers and high-speed air compressors for fuel cells [23,24]. Pattnayak et al. developed a new bore for high-performance behaviors of self-acting GFBs based on numerical investigations, and compared it with the results of conventional bump foil/rigid bore aerodynamic bearings [25]. Ganaïet et al. proposed a method to reduce friction and improve the dynamic performance of a self-acting air foil journal bearing, using a texture with rectangular dimples [26]. Samanta et al. reviewed the key technological innovations in structural foil designs that leverage the stiffness and damping of foil structure for high-speed and high-load applications [27]. Liu X. et al. built a test rig for thrust gas bearings and measured the temperature under different working conditions [28]. Kumar et al. presented an overview of the work completed in the past few decades regarding the development of numerical models. They listed the efforts of several researchers around the world to conduct experimental investigations for predicting and analyzing the thermohydrodynamic behavior of gas foil bearings at different operating conditions [29].

Theoretical approaches used to investigate the performance of BFJBs have been discussed in various references. Salehi et al. explored the static performance and temperature field of a GFB with the Reynolds equation, the air film energy equation and the simple elastic base model [30]. Peng and Khonsari proposed a THD model to investigate the static performance of foil air bearings. The bearing structure adopts a simple elastic base model, and the field distributions of the film pressure and temperature are obtained by coupling the Reynolds equation and the energy equation [31]. Zhou Y. et al. simplified the interaction force in the bearing into the form of a spring, realizing the decoupling of the complex rotor system [32]. Feng K's team presented a numerical model for the 3D thermo-hydrodynamic analysis of sparse mesh bump-type foil bearings on air films, taking into account thermal convection in the cooling air, the thermal expansion of the bearing components, and the changes in material properties due to thermal variation. The lubrication model of the thrust bearing has been simultaneously coupled with the generalized Reynolds equation, film thickness equation, energy equation, viscosity equation, solid heat conduction equation, and solid thermal expansion equation [33,34]. Andres et al. developed a theoretical model

that considers thermoelastic deformation, thermal expansion, and the centrifugal growth of the rotor [35,36]. Lai T. et al. analyzed foil bearing stability with the Timoshenko beam element, which is an accurate and fast method [37].

There is dry friction between the rotor shaft and the top foil of the BFJB before the turbocharger rotor lift-off, which causes the temperature of the rotor shaft and the elastic support foil to rise sharply. The elastic support foil will fail due to excessive temperature [38]; this can easily cause unnecessary losses and even lead to accidents involving machine crashes and fatalities [39]. Although many investigations have been conducted on the temperature characteristics of BFJBs, there is no suitable method to evaluate the state of oil-free turbochargers in real time. Considering these analyses above, this paper proposes a method which evaluates the performance and predicts the life cycle of BFJBs using temperature characteristics. The novelty of this work lies in the exploration of BFJB thermohydrodynamic characteristics as the key element of the proposed experimental investigation. A new BFJB test rig and various test BFJBs were designed to monitor the temperature field. The experimental results and the numerical calculations were compared to verify the method. The presented method can be used to guide BFJB design and predict the life of BFJBs. The rest of this paper is organized as follows: in Section 2, a numerical model of the BFJB considering the thermal deformation of foil is established. In Section 3, a new BFJB test rig and various test BFJBs are designed to measure the thermal characteristics. Section 4 presents the experimental results and compares them with numerical calculations to verify the feasibility of the proposed experimental method. The last section presents the conclusions of this paper.

2. Numerical Model of BFJBs

2.1. Energy Equation

A large amount of heat is generated when the supercharger rotor is running at high speed, and the prediction of the gas film temperature in the BFJB requires a simultaneous solution to the Reynolds equation and the energy equation. The Reynolds equation and the energy equation are both functions of pressure and temperature. It is very complicated to solve the full energy equation of the temperature field in the bearing [40]. Under non-isothermal conditions, the steady-state Reynolds equation for the gas film can be presented as [41]:

$$\frac{1}{R^2} \frac{\partial}{\partial \theta} \left(\frac{ph^3}{12\mu T} \frac{\partial p}{\partial \theta} \right) + \frac{\partial}{\partial y} \left(\frac{ph^3}{12\mu T} \frac{\partial p}{\partial y} \right) = \frac{\omega}{2} \frac{\partial}{\partial \theta} \left(\frac{ph}{T} \right) \quad (1)$$

where μ denotes the gas viscosity (Pa·s), T denotes the gas film temperature ($^{\circ}\text{C}$), x denotes the circumferential direction, y denotes the bearing width direction; z denotes the gas film thickness direction; and ω denotes the rotor angular velocity (rad/s).

There is a certain relationship between the viscosity of the gas and the temperature [29]. This can be presented as:

$$\mu = a(T + T_{ref}) \quad (2)$$

where $a = 4 \times 10^{-8}$ and $T_{ref} = 458.75 \text{ }^{\circ}\text{C}$.

The heat transfer of the gas film is described by the energy transfer equation, and the process is partially simplified according to the actual heat transfer [42]:

- (1) The thermal conductivity of the BFJB in the x direction is negligible compared with the convective heat transfer;
- (2) The thickness of the gas film is of micrometer-scale, so the main form of energy transfer along the z direction is heat conduction. The simplified energy equation is provided as:

$$\rho c_p \left(u \frac{\partial T}{\partial x} + v \frac{\partial T}{\partial y} + \omega \frac{\partial T}{\partial z} \right) = k \left(\frac{\partial^2 T}{\partial y^2} + \frac{\partial^2 T}{\partial z^2} \right) + u \frac{\partial p}{\partial x} + v \frac{\partial p}{\partial y} + \mu \left(\left(\frac{\partial u}{\partial z} \right)^2 + \left(\frac{\partial v}{\partial z} \right)^2 \right) \quad (3)$$

where c_p (J/(kg·K)) denotes the specific heat capacity of the gas at constant pressure, k (W/(m·K)) denotes the thermal conductivity of the gas, u (m/s) denotes the velocity in the x direction of the gas film, v (m/s) denotes the velocity in the y direction of the gas film, and ω (m/s) denotes the velocity in the z direction of the gas film. The schematic diagram of the BFJB is shown in Figure 1.

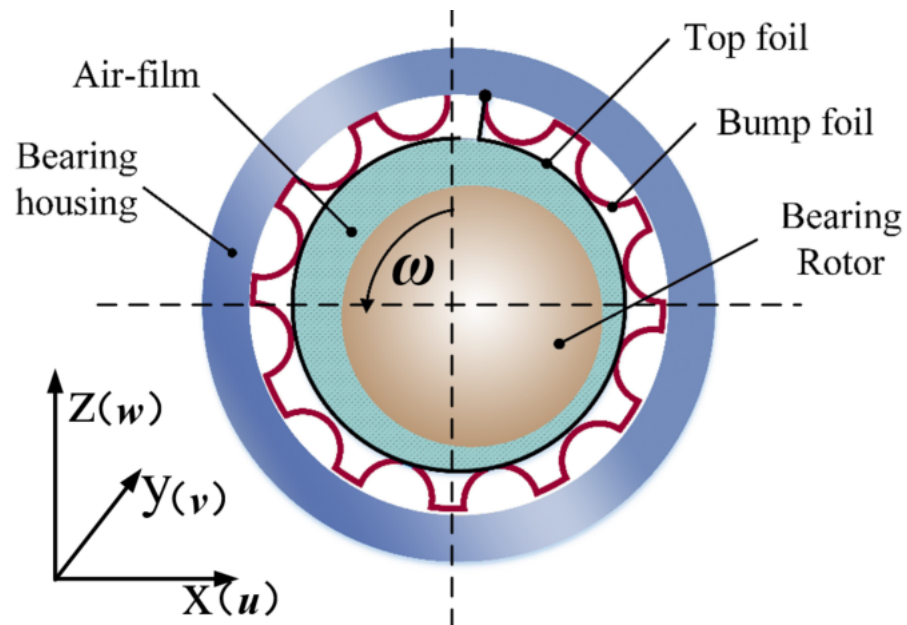


Figure 1. Schematic diagram of the BFJB.

The rotor growth at high temperature and high rotational speed significantly influences the air film because of its thinness. To reasonably predict the temperature field, the thermal and centrifugal effect on rotor growth cannot be ignored. The film thickness can be presented as:

$$h = c(1 + \varepsilon \cos) + (p - p_a) \cdot s / k_b - \Delta C_t - \delta_c \quad (4)$$

where c (m) denotes the initial air-film gap; s (m) denotes the foil pitch; k_b (N/m²) denotes the axial unit foil length stiffness; and δ_c (m) denotes the centrifugal growth of the rotor.

The thermal expansion of the bearing system is represented by ΔC_t (m):

$$\Delta C_t = \delta_s + \delta_f - \delta_h \quad (5)$$

where δ_s denotes the thermal expansion of the rotor; δ_f denotes the thermal expansion of the bump foil structure; and δ_h denotes the thermal expansion of the bearing top foil.

The centrifugal growth for the rotor due to high-speed rotation is calculated as:

$$\delta_c = \frac{\rho R^3 \omega^2}{4E} (1 - \nu) \quad (6)$$

where E denotes the elasticity modulus; ρ denotes the material density; ν denotes the Poisson ratio; and R denotes the rotor radius.

The gas film energy boundary conditions are [43]:

$$\begin{aligned} T|_{z=h_{\min}} &= T_{\text{rotor}} \\ T|_{z=h_{\max}} &= T_{\text{top}} \\ T|_{\text{steady}} &= T_{\text{air}} \end{aligned} \quad (7)$$

where T_{rotor} denotes the shaft temperature; T_{top} denotes the top foil temperature; and T_{air} denotes the air gap temperature.

In this paper, the finite difference method and the Newton–Raphson method are combined to solve the model. It can be seen from Equations (1)–(7) that the non-isothermal Reynolds equation, the gas film energy equation, and the gas film thickness equation are coupled with each other; therefore, ignoring the influence of assumptions, a steady-state convergent solution can be obtained in an iterative manner [44].

2.2. Thermohydrodynamic (THD) Model of BFJBs

In this section, Figure 2 presents a schematic of the THD model for the BFJB consisting of the bearing shell, bump foil, top foil, and rotating shaft [45]. According to the working principle of BFJBs, the heat generated from the viscous shearing in the air film is partly converted into the heat energy of the air film, among other components; moreover, these other parts diffuse into the atmosphere in the form of heat energy through the top foil, bump foil, bearing housing, and rotor. Compared with the bearing structure size, the thickness of the air film can be ignored, so the proportion of heat diffused into the environment by the air film is very small. Because the top foil is very thin, the heat transfer area in the lateral direction is negligible; therefore, the lateral heat transfer of the top foil can be ignored. Assuming a uniform rotor temperature distribution, the rotor temperature and the top foil temperature are used as boundary conditions for the film temperature calculation.

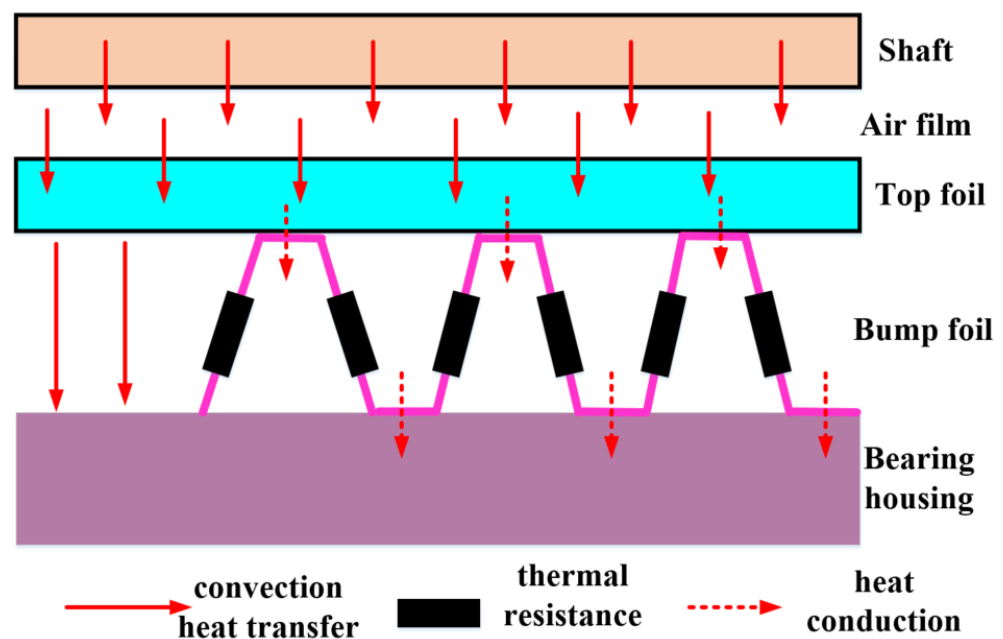


Figure 2. Schematic diagram of the heat transfer model of a BFJB.

As can be seen from Figure 2, the heat generated by the air film is divided into three parts. Part of the heat is transferred to the bump foil in the form of heat conduction through the top foil. Then, it is transferred to the air gap between the bump foil and the bearing seat in the form of thermal convection and, finally, it is diffused into the surrounding environment through the bearing seat. Another part of the heat is transferred directly through the top foil in the form of thermal convection into the air gap between the top foil and the bearing seat, and then the heat is dissipated into the environment through the bearing seat. The third part of the heat is transferred to the air gap between the top foil and the bearing seat in the form of thermal convection through the top foil, and then the heat is conducted to the bearing seat through the bump foil, and finally diffused into the environment through the bearing seat [46].

The thermal resistance of each part can be calculated using Equation (8).

$$R = \frac{h}{kA} \quad (8)$$

The thermal resistance of each part is calculated in Equation (8), where k (W/(m·K)) denotes the thermal conductivity, A (m²) denotes the heat transfer area, R (K/W) denotes the thermal resistance, and h denotes the film thickness in the heat transfer direction.

The total thermal resistance can be calculated as [38]:

$$R_{tot} = R_T + \frac{1}{\frac{1}{R_{G1}} + \frac{1}{(R_{sec} + R_{G2})} + \frac{1}{R_B}} + R_H + R_{cf} \quad (9)$$

where R_T denotes the thermal resistance of the top foil, R_G denotes the thermal resistance of the air gap of the bump foil, R_s is the thermal resistance of the bump foil, R_H is the thermal resistance of the bearing shell, R_{sec} is the thermal resistance of the top foil contact, and R_{cf} is the thermal resistance during natural convection heat dissipation.

When the heat transferred from the air film to the top foil and the heat transferred from the top foil are in dynamic equilibrium, the bearing temperature comes to a steady state. According to this equilibrium relationship, the heat balance equation can be presented as [43]:

$$-k_a A \frac{\partial T_F}{\partial z} = \frac{T_0 - T_F}{R_{tot}} \quad (10)$$

After the dimensionless Formula (10), we can get:

$$\bar{T}_F + \gamma \frac{\partial \bar{T}_F}{\partial \bar{z}} = 0 \quad (11)$$

where $\gamma = -\frac{k_a A R_{tot}}{h}$.

The supercharger uses a solid rotor; the heat is transferred from the gas film to the rotor, and then diffused by the rotor into the environment. Because of the high rotational speed of the rotor, the rotor temperature can be further assumed to be equal in the circumferential direction [24], and the temperature situation of the rotor can be simplified as a one-dimensional temperature model distributed along the axial direction [47,48].

$$Q_{conv}^j + \frac{k_R A_c}{\Delta y} (T_R^{j+1} + T_R^{j-1} - 2T_R^j) - \frac{T_R^j - T_0}{R_{in}} = 0 \quad (12)$$

$$Q_{conv}^j = -k_a A_{R,i} \sum_i \frac{\partial T}{\partial z} \Big|_{z=h} \quad (13)$$

In the formula, k_R (W/(m·K)) is the thermal conductivity of the rotor; A_c (m²) is the cross-sectional area of the rotor; T_R (K) is the rotor temperature; and R_{in} (K/W) is the thermal resistance in the thickness direction of the rotor shaft.

2.3. Calculation Process

In this paper, the Finite difference method and the Newton–Raphson method are combined to solve the model and the Taylor series expansion method is used to construct the difference scheme. In a homogeneous grid, Δx represents the space step in the x direction, and f represents an arbitrary function. In order to get the difference quotient of the partial derivatives of the function f , with respect to x , expand into a Taylor series in the neighborhood of x_i .

$$f_{i+1} = f_i + \frac{\partial f}{\partial x} \Big|_i \Delta x + \frac{\partial^2 f}{\partial x^2} \Big|_i \frac{\Delta x^2}{2!} + \frac{\partial^3 f}{\partial x^3} \Big|_i \frac{\Delta x^3}{3!} + \frac{\partial^4 f}{\partial x^4} \Big|_i \frac{\Delta x^4}{4!} + HOT \quad (14)$$

$$f_{i-1} = f_i - \frac{\partial f}{\partial x} \Big|_i \Delta x + \frac{\partial^2 f}{\partial x^2} \Big|_i \frac{\Delta x^2}{2!} - \frac{\partial^3 f}{\partial x^3} \Big|_i \frac{\Delta x^3}{3!} + \frac{\partial^4 f}{\partial x^4} \Big|_i \frac{\Delta x^4}{4!} + HOT \quad (15)$$

The aim of the finite difference method is essentially to approximate solutions to differential equations by replacing the derivatives in the differential equations with finite difference approximations. The grid of finite differences covers a continuous area, and the finite difference decomposition is defined at the nodes. Convert a continuous space to a discrete space grid with two sets of parallel lines containing $I \times J$ rectangular subdomains. The coordinates of the grid intersection can be presented as:

$$x = i\Delta x(i = 0, 1, \dots, I), y = j\Delta y(j = 0, 1, \dots, J) \tag{16}$$

$$\Delta x = X/I \tag{17}$$

$$\Delta y = Y/J \tag{18}$$

where Δx and Δy represent the space steps in the x and y directions, respectively, as shown in Figure 3.

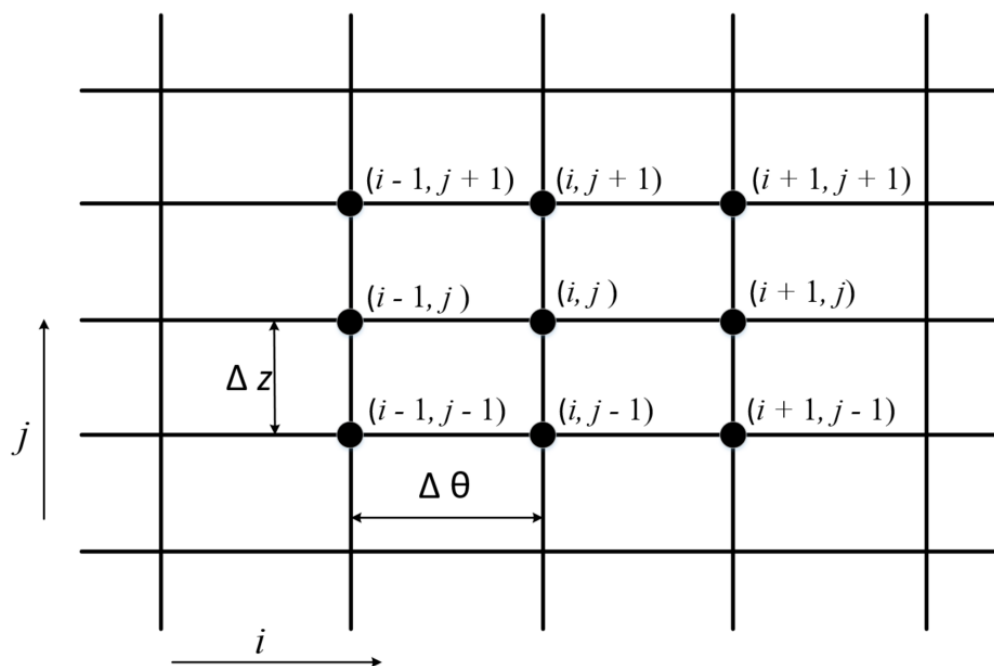


Figure 3. A portion of the computational grid of the film gap.

After finite difference processing, the Reynolds equation of the BFJB is transformed into a higher-order nonlinear equation system, which is difficult to solve directly. Therefore, the Newton–Raphson method is used to solve it iteratively. Newton–Raphson is a method of approximately solving equations in real and complex fields, and $(I - 2) \times (J - 2)$ equations can be obtained.

The calculation flow is shown in Figure 4.

In this paper, the BFJB is discretized into 125×125 points. This solves a system of linear equations, with 15,625 equations consuming a lot of time. The solution tool used in this research was the MATLAB commercial package, and the workstation was equipped with an Intel i7-1800H processor and 32 GB of memory, which manufactured by Dell Inc. in North America. Therefore, it could perform iterative calculations quickly and improve work efficiency.

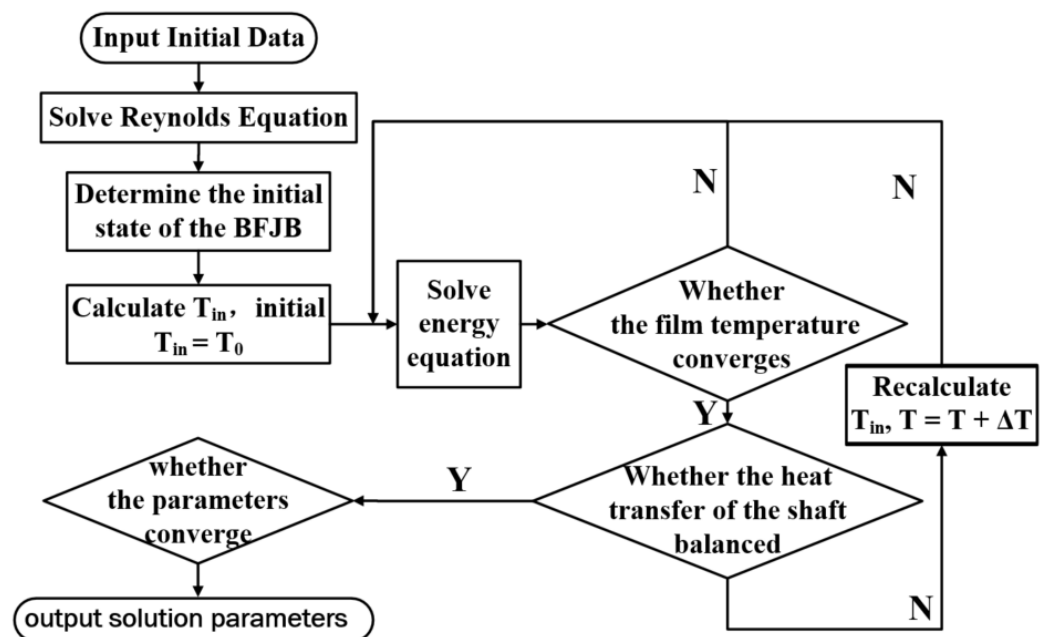


Figure 4. Flow chart of temperature calculation.

3. Experiments

3.1. Description of the Test BFJB

The test BFJB structure consisted of a top foil, bump foil and a bearing housing which was more stable than a traditional rigid bearing [49]. The support stiffness of the BFJB was determined by the structural parameters (as shown in Figure 5) [50]. When the shaft was stationary, the support stiffness of the BFJB was symmetrical. When the rotor turned from the free end of the foil to the fixed end, the top foil and the shaft formed a wedge-shaped area to generate aerodynamic pressure, and the support stiffness of the bump foil was no longer symmetrical.

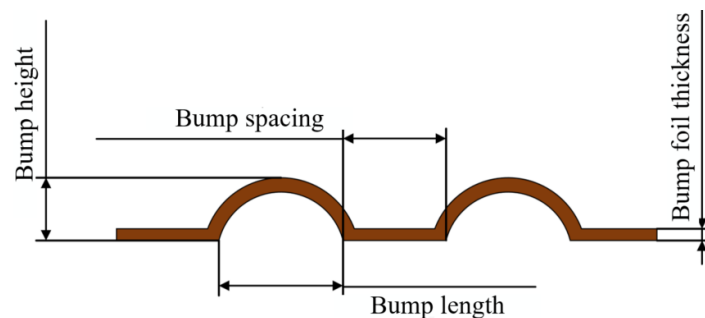


Figure 5. Configuration of bump foil.

Figure 6 demonstrates the production process of the experimental BFJB. The bump foil was stamped and formed by the bulging process, and the material was X750 stainless steel (Figure 6a). To obtain three different bump foils, firstly, stainless steel was cut into strips with a width of 6 mm and a length of 102 mm (Figure 6b). Then, corresponding bulging molds (Figure 6c) were made according to the structural parameters of each bump foil. Thirdly, the strips were placed in the bulging molds (Figure 6d). The semi-finished bump foil after bulging is shown in Figure 6e. Finally, the semi-finished BFJB was heated at 650 °C for 4 h and then cooled to room temperature in air (Figure 6f). The product after heat treatment is shown in Figure 6g.

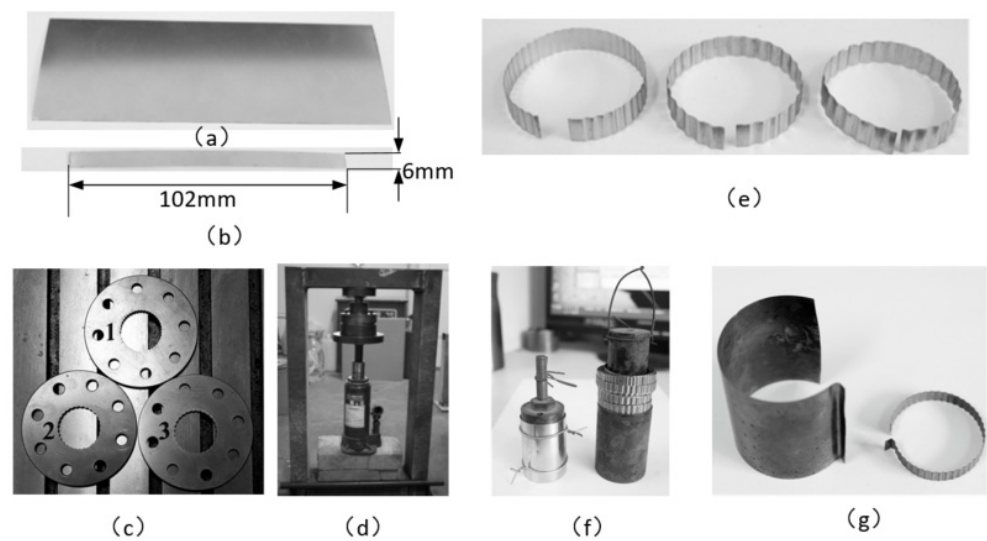


Figure 6. Test bearing preparation. (a) X750 Stainless steel; (b) Cut stainless steel bars; (c) Bump foil bulging model; (d) Bump foil bulging device; (e) Bulge-finished bump foil; (f) Foil heat treatment; (g) Finished bump foil.

The structure of the experimental BFJB is shown in Figure 7. The BFJB used in the test had two narrow grooves with a width of 0.2 mm in the bearing shell. The bump foil and the top foil were fixed on the grooves by an HT-CPS high-temperature structural adhesive, and the other end was free (Figure 7a). The HT-CPS high-temperature structural adhesive working temperature was $-196\sim 980\text{ }^{\circ}\text{C}$ and the shear strength and the tensile strength after curing were 86 MPa and 38.5 MPa, respectively, which fully met the requirements of the BFJB. It should be noted that the distance between the bending point of the foil and the first bump must be consistent. This determines that all bumps are aligned in straight lines after the seven bump foils are installed. Symmetry is an important aspect of such structures, as shown in Figure 7b,c. The prepared BFJB object is shown in Figure 7d.

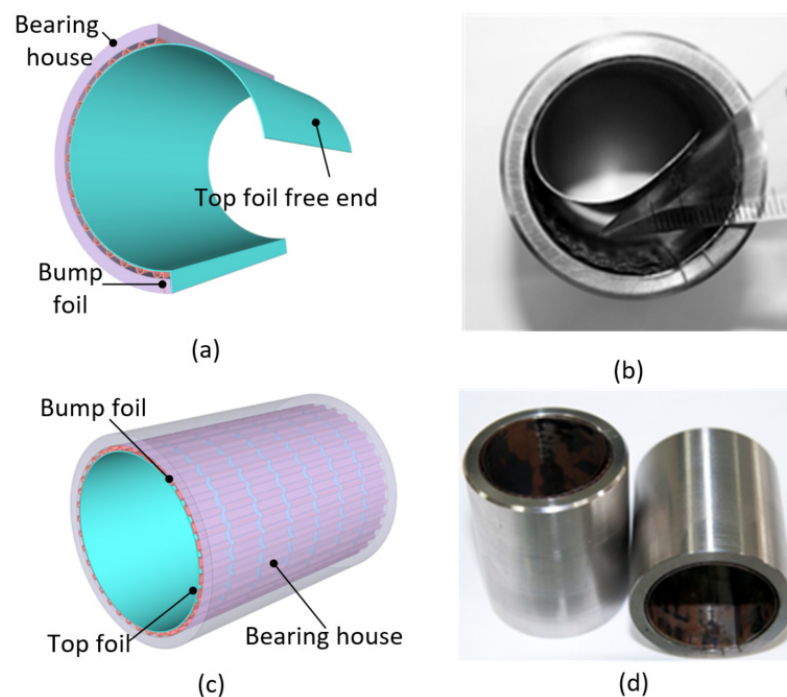


Figure 7. Installation structure of experimental bearing. (a) Assembly structure diagram; (b) Physical drawing of assembly structure; (c) Assembly structure perspective; (d) Test bearing.

The main parameters of the test bearings are shown in Table 1. No. 1, No. 2 and No. 3 test BFJBs had top foil with a thickness of 0.1 mm. No. 4, No. 5 and No. 6 test BFJBs had top foil with a thickness of 0.12 mm. The rest of the parameters were exactly the same.

Table 1. Main parameters of the bearings.

Number	B1	B2	B3	B4	B5	B6
Top foil thickness (mm)	0.1	0.1	0.1	0.12	0.12	0.12
Nominal clearance (μm)	76	76	76	56	56	56
Bump length (mm)	2	2.5	3	2	2.5	3
Bump foil thickness (mm)				0.1		
Bump spacing (mm)				0.7		
Bump height (mm)				0.5		
Bearing diameter (mm)				32		
Axial length (mm)				48		
Poissons ratio				0.29		
Elasticity modulus (Gpa)				213		

In the initial state, the BFJBs and connecting pieces weighed 1225 g. The different load tests carried out in this paper were based on the initial state.

3.2. Description of the Test Bench

This experiment adopts a self-designed test bench suitable for BFJB research. The components used in the test bench are shown in Table 2, and Figure 8 shows the mounting position of the relevant components.

Table 2. Test bench components.

Title	Performance	Function
Electric spindle	Max. speed 90,000 r/min	Drive shaft to rotate
SJH300 Inverter	Max. power 7.5 kW frequency 1500 Hz	Adjust the speed
HZ-8500 Eddy Current Displacement Sensor	range 1.5 mm, Nominal sensitivity frequency 4 kHz	Measure the displacement of the bearing during operation
Tension sensor and its accessories	range 20 kg precision 0.1% voltage signal 0–5 V	Measure the resistance torque of the bearing
Type K thermocouple	range 0~400 °C	Measure the bearing housing temperature
Electric Glow Plug		Different bearing temperatures available
data collection system	Max. frequency 4 kHz	Collect and record bearing temperature
work platform	800 mm × 800 mm thickened cast iron	Reduce the impact of vibration on EX results

The measurement principle of the BFJB test bench is shown in Figure 9. The motorized spindle was used to drive the rotor, and the bearing and the bearing seat were suspended on the shaft. The bearing resistance torque was converted into a tensile force measurement through a measuring rod fixed on the bearing seat, and the bearing load was increased by adding weights on the left side. An eddy current displacement sensor with a range of 0.5 mm was used to measure the rotational speed of the shaft, and two eddy current displacement sensors were used to measure the bearing displacement without contact,

which were mounted symmetrically on both sides of the shaft [51]. The data from the two displacement sensors within 1 s were acquired as soon as the BFJB had fully lifted off and reached a steady state. These were transformed into horizontal and vertical coordinate dimensions. According to these coordinate dimensions, we drew the BFJB journal orbits and obtained the lift-off time.

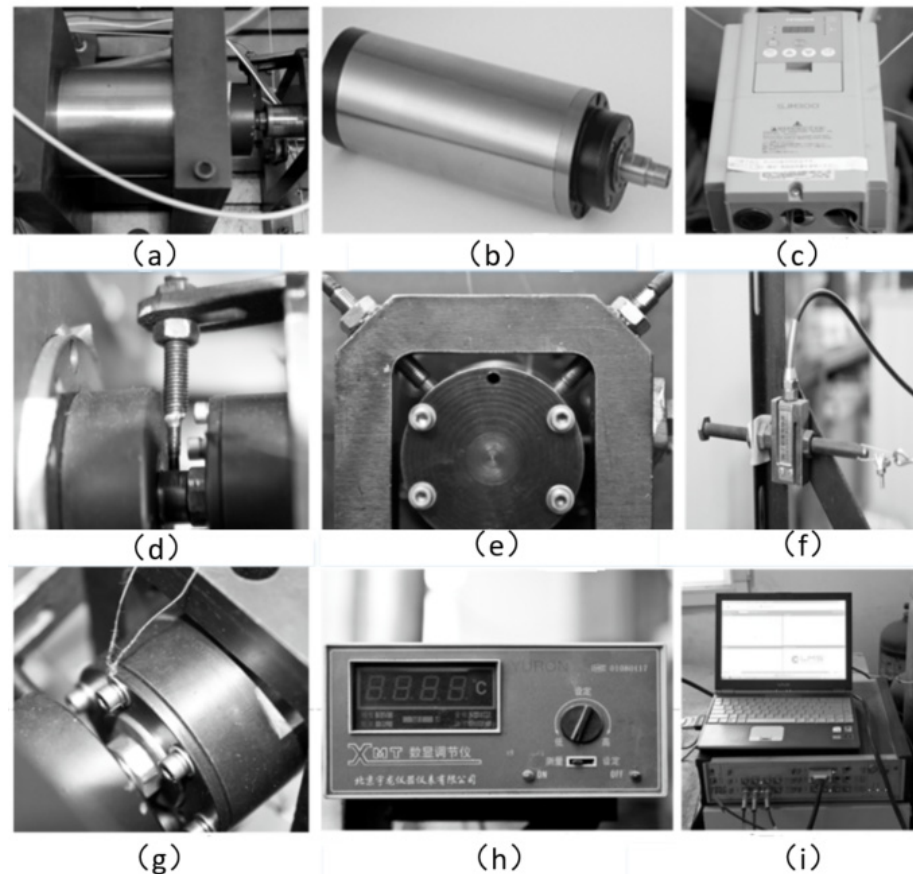


Figure 8. Configuration of the test bench. (a) Rotor system; (b) Electric spindle; (c) Inverter; (d) Eddy current speed sensor; (e) Eddy current displacement sensor; (f) Resistance torque sensor; (g) K-type thermocouple; (h) Temperature indicator; (i) Data collection system.

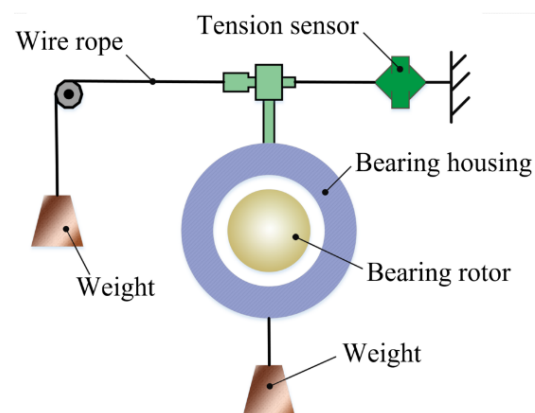


Figure 9. Schematic of the BFJB test bench.

In this test bench, the K-type thermocouple on the back of the bump foil and a digital display instrument were used to measure the temperature of the film. In this paper, the temperature collected by the thermocouple was approximated in regard to the temperature

of the gas film [25]. Figure 10 shows the installation positions of 7 K-type thermocouples, which were symmetrically distributed along the middle of the BFJB to both ends.

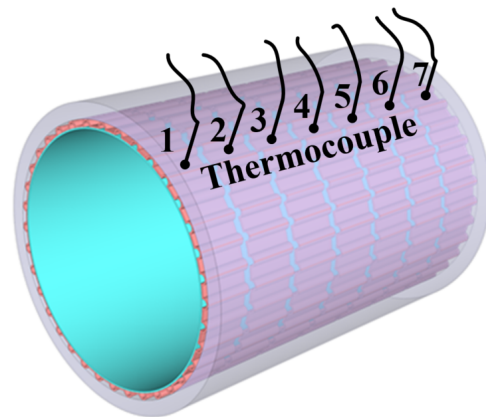


Figure 10. Location of the K-type thermocouple.

Figure 11 shows the BFJB test bench. All components of the test bench were arranged on an 800 mm × 800 mm working platform. To avoid the vibrations of the test bench affecting the test results, the working platform was made of thickened cast iron to minimize vibration.

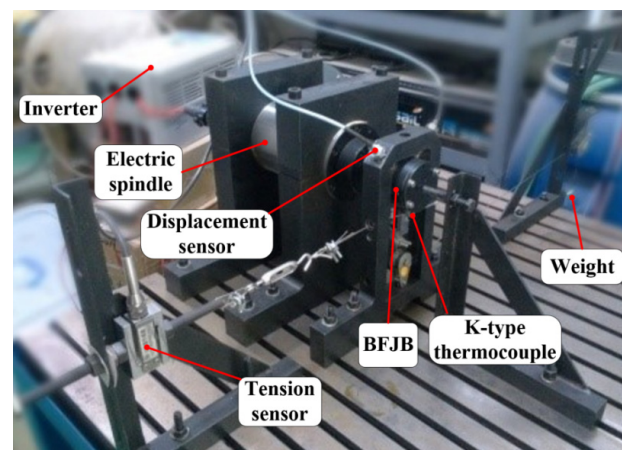


Figure 11. Bump foil radial air bearing test bench.

4. Results and Discussion

In order to verify the temperature characteristics of BFJB, the numerical results were compared with the experimental results. In this section, EX is the experimental result and NU is the numerical calculation result.

4.1. Influence of the Increase in Speed and Load on the Temperature Rise in the BFJB and the Shaft

Figure 12 shows the relationship between the BFJB temperature and the rotor speed when no load was applied, as measured by the first thermocouple in Figure 10. It can be seen that the rotational speed increased from 20,000 rpm to 90,000 rpm as the temperature of the gas film increased almost linearly. The results show that the rotation speed was lower than 65,000 rpm, and the experimental results were in good agreement with the numerical results. When the rotation speed exceeded 65,000 rpm, the EX temperature of the gas film fluctuated frequently. After analysis, it was concluded that this may have been related to the vibration of the rotor at the critical speed, which caused the rotor to make contact with the top foil, resulting in temperature fluctuations [52].

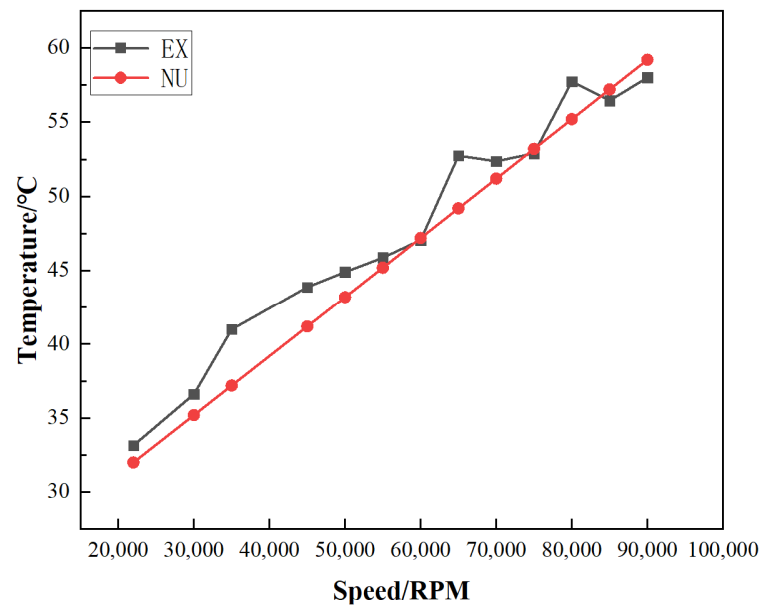


Figure 12. The effect of rotational speed on the maximum film temperature.

Figure 13 shows the variation of the maximum steady-state temperature of the test bearing with the load. A total of six load points of 16 kg were measured in the test. The load point of 0 kg does not mean that the load of the BFJB was 0, but means that the BFJB, bearing seat, wire rope and resistance torque measuring rod composed a total of 1225 g. The loads indicated in the figure are additional loads. The changes in the maximum bearing temperature with loads at three different speeds of 30,000 rpm, 50,000 rpm and 70,000 rpm were analyzed, and the applied load increased from 10 to 60 N. Compared to the NU and EX, the maximum temperature of the gas film gradually increased as the load increased from 10 to 60 N, but the increased range was not large. Compared with the changes in the film temperature caused by the rotation speed, the change in the film temperature caused by the load was relatively small. The temperature measured in the experiment was slightly higher than the temperature calculated by the numerical model.

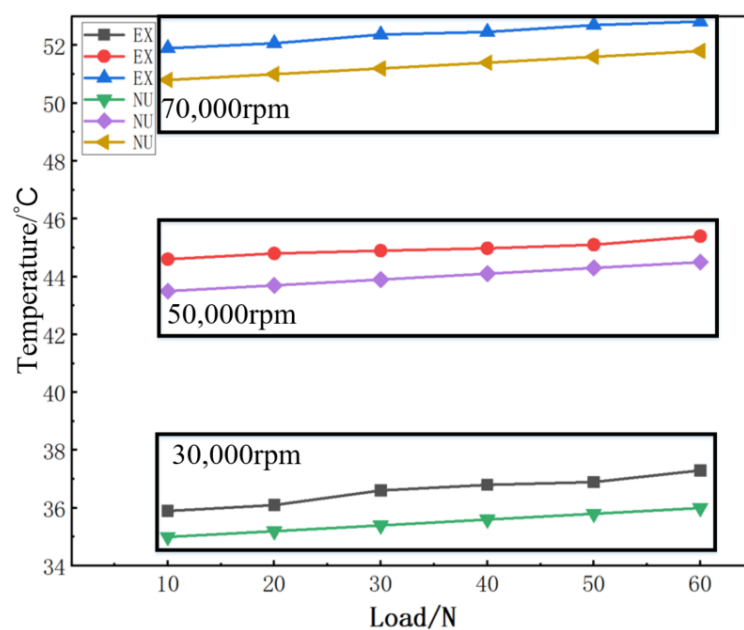


Figure 13. Effect of load on maximum bearing temperature.

As mentioned above, the supercharger adopted a solid rotor, and the heat was transferred to the rotor by the gas film, and then diffused by the rotor into the environment. The working speed of the rotor was relatively high, and it can be further assumed that the rotor temperature was equal in the circumferential direction. Thereby, the temperature of the rotor can be simplified as a one-dimensional temperature model distributed along the axial direction. The steady-state temperature measured by the thermocouples, as shown in Figure 10, represents the temperature distribution of the shaft along the axial direction. Figure 14 shows the change in the temperature of the shaft with the rotation speed, and seven temperature points in the axial direction were measured. It can be seen that the temperature in the middle of the rotor was the highest, which was then distributed symmetrically to both ends. After analysis, it was concluded that this was because the two ends of the rotating shaft exchanged heat with the environment, resulting in a lower temperature than the middle part of the rotor.

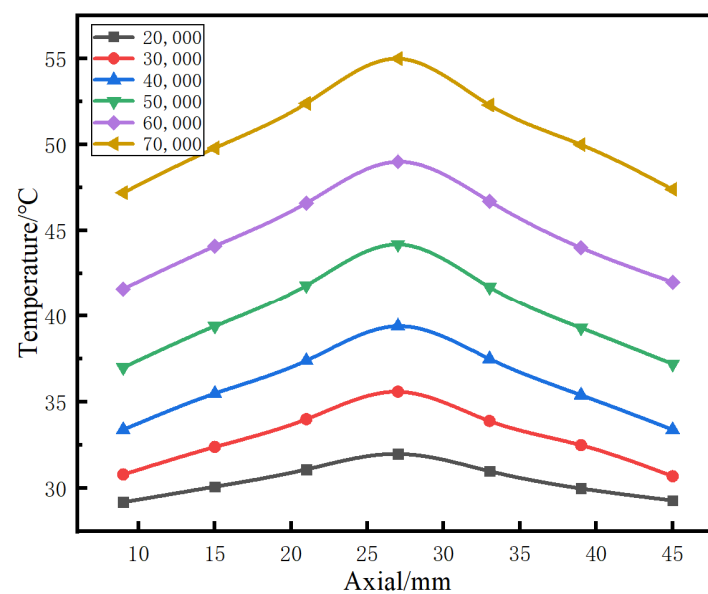


Figure 14. Axial temperature distribution of the rotor.

4.2. Influence of Structural Parameter Changes on the Performance of BFJB

Figure 15 shows the relationship between the rotational speed, the frictional resistance torque T , and the time measured in the experiment. It can be seen that the shaft started to rotate when the resistance torque of the bearing reached the maximum and, as the rotation speed of the shaft increased, the resistance torque of the BFJB gradually decreased. When the speed of the shaft reached a certain value, the resistance torque of the bearing tended to be stable; the resistance torque of the bearing did not change with rotating speed change, and the resistance torque of the bearing was very small at this time, with almost no resistance. The speed at which the BFJB resistance torque was in a steady state was defined as the lift-off speed of the BFJB. During the stopping process, when the speed dropped to the point where the bearing resistance torque was no longer stable, this speed of the BFJB was defined as the stop-contact speed. The lift-off speed and stop-contact speed measured by this method were slightly higher than other methods [53].

Figure 16 shows the effect of bearing structural parameters on lift-off speed. Taking No. 1–3 BFJBs as a group, and No. 4–6 BFJBs as the other group, it can be seen that the lift-off speed of the bearing under the same load increased with the increase in the width of the bump foil. As the width of the bump foil increased from 2 mm to 2.5 mm, and then increased from 2.5 mm to 3 mm, the lift-off speed of the BFJB increased by 5320 r/min and 13,417 r/min, respectively. Therefore, it is considered that the influence of the bump width on the support stiffness of the BFJB was nonlinear. Dividing B1 and B4 B2 and B5, B3 and B6 into three groups, it can be seen that the lift-off speed of the No. 1, 2, and 3 test BFJBs

with 0.1 mm thickness top foil under each load was higher than that of No. 4, 5, and 6 test BFJBs with 0.12 mm thickness top foil. This result is consistent with the analysis of the influence of the width of the bump foil on the bearing lift-off speed. When the thickness of the top foil changed from 0.1 mm to 0.12 mm, the lift-off speed of the bearing decreased by an average of 5771 r/min. Comparing the influence of the thickness of the top foil on the bearing stiffnesses to the width of the bump foil on the bearing stiffnesses, it was found that the width of the bump foil had a significant effect on the bearing stiffness.

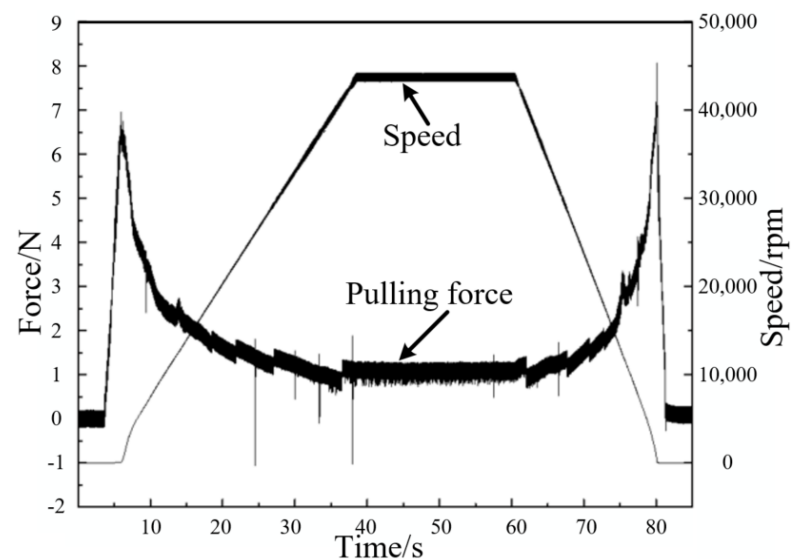


Figure 15. Resistance and speed of the BFJB during lift-off and stop-contact.

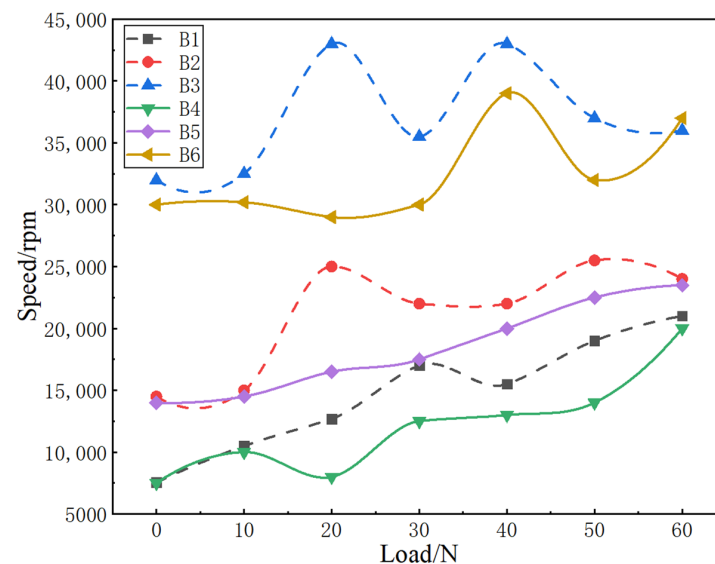


Figure 16. Influence of bearing structure parameters on lift-off speed.

Figure 17 shows the effect of the width of the bump foil on the maximum film temperature. From the test of No. 1–3 BFJBs, it can be seen that with the increase in the width of the bump foil, the maximum temperature of the air film gradually increases under the same load, but the increase was not large. From the EX of No. 4–6 BFJBs, the same rules were observed. Comparing No. 1–3 BFJBs and No. 4–6 BFJBs in Figure 16, it can be seen that with the increase in the thickness of the top foil, the gas film temperature decreased slightly. After analysis, it was concluded that this could be explained by the variation in the stiffness of the elastic support structure to the width of the bump foil or the thickness of the top foil.

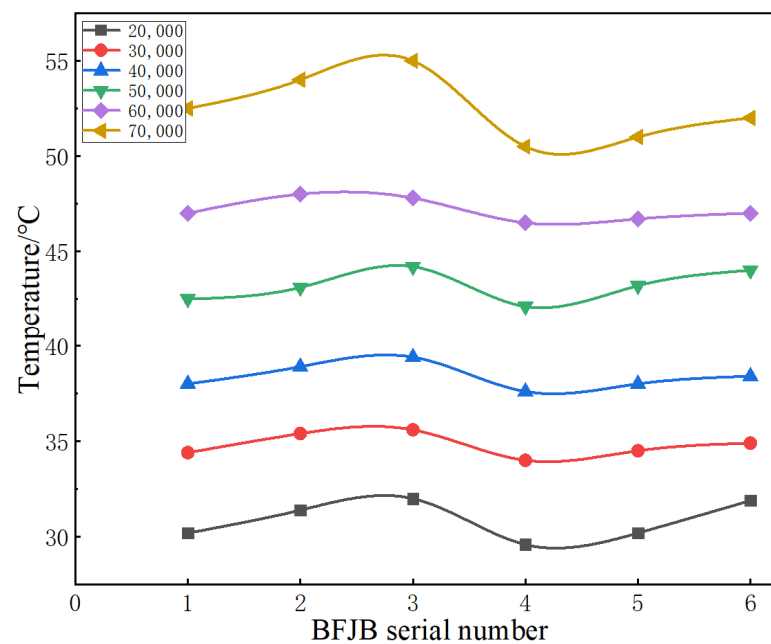


Figure 17. Influence of different structural parameters on gas film temperature.

Figure 18 shows that the No. 3 BFJB was accelerated to stability without additional load at room temperature, and then the bearing was heated to different specified temperatures with glow plugs. Subsequently, the speed of the electric spindle of the test bench gradually reduced until the measurement torque was unstable. Recording the speed at this time as the stop-contact speed at this temperature, it can be seen that the lift-off speed was slightly different for each measurement, which was caused by the different room temperatures and measurement deviation during the measurement. The stop-contact speed was always higher than the lift-off speed, and the stop-contact speed gradually increased with the temperature increases. The results can be explained by the thermal expansion of the bearing with the increase in temperature and the reduction in the bearing capacity with the decrease in the air gap and the degradation of the stiffness of the air film, resulting in the gradual increase in the stop-contact speed. Therefore, superchargers of APEs should be gradually cooled down during the stop to avoid the increased wear caused by excessive contact speed.

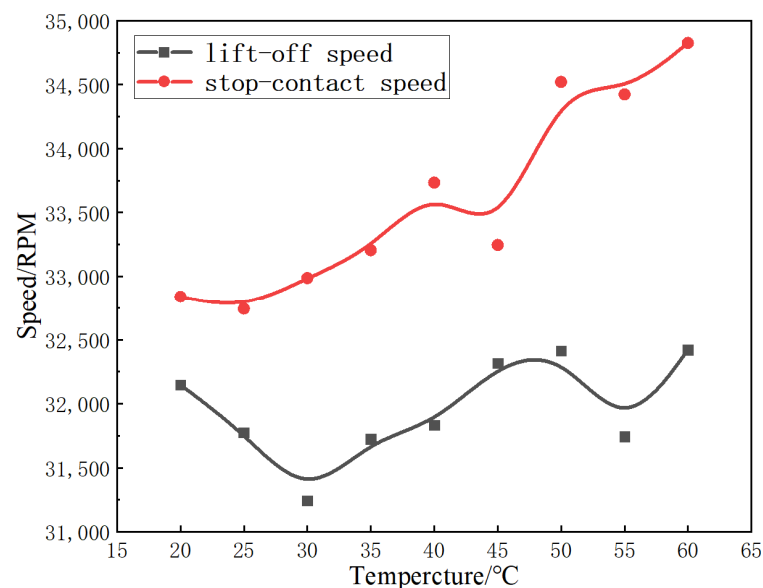


Figure 18. Variation of stop-contact speed with bearing temperature.

4.3. The Process of Stop-Contact under Different Load Conditions

Figure 19 shows the variations in the stop-contact speed and the spend time with the load measurements of the No. 3 bearing. Firstly, the rotor system was accelerated to 40,000 rpm at room temperature and the rotating shaft was in lift-off, at this time, to stop the rotor drive. It can be seen that the downtime was gradually shortened as the bearing load increased. When the speed was lower than the stop-contact speed, the rotor decelerated with the load increase. After analysis, it was found that the frictional resistance increased when the rotor was in sliding contact with the bearing as the load increased. The speed drop acceleration was not large before reaching the stop-contact speed, which can be explained by the film temperature rising with the load increase, resulting in the thermal expansion of the bearing and an increase in the stopping contact speed with increasing load.

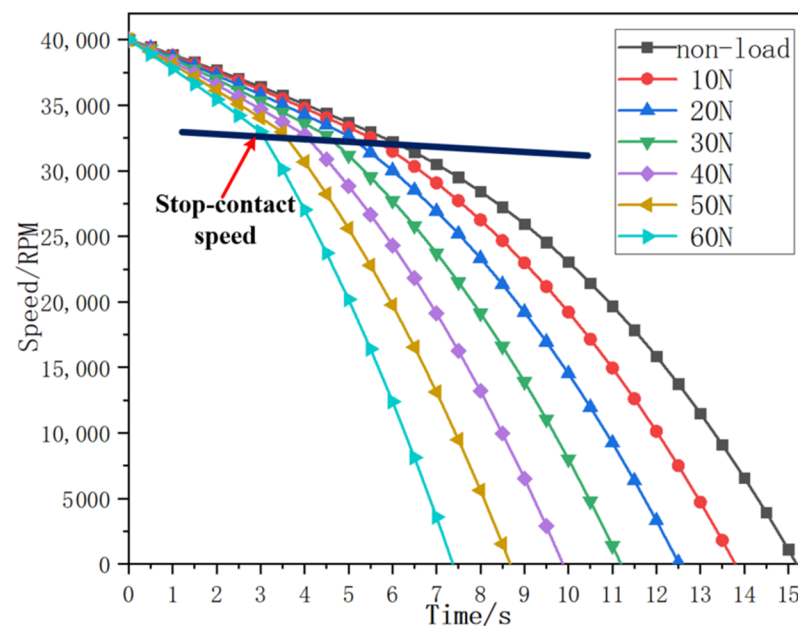


Figure 19. Time taken to stop under different load conditions.

5. Conclusions

In this paper, both experimental and theoretical methods were applied to investigate the thermal characteristics of BFJBs, and a method to evaluate the state of BFJBs by measuring the temperature of the gas film was proposed. Detailed conclusions are as follows:

- (1) In our study, with the increased width of the bump foil, the support stiffness of the BFJB decreased, the lift-off speed of the BFJB accelerated and climbed, and the magnitude of the temperature rise increased. These results can be explained by the fact that the stiffness of the elastic support structure changed with the width of the bump foil or the thickness of the top foil, resulting in the lift-off speed change;
- (2) In order to avoid damage to the bearing caused by excessive dry friction, which affects the safety of turbochargers, this paper proposed a method of monitoring temperature to predict BFJB performance. The fault of the supercharger can be diagnosed when the temperature suddenly changes, and the temperature of the supercharger can be managed according to temperature characteristics. During the stop process of an APE with a turbocharger, the power should be slowly reduced to cool the supercharger sufficiently. When the rotor system drops to the stop-contact speed, an additional load can be taken to accelerate the rotor system to stop. These measurements can avoid long-term dry friction and prolong bearing life;
- (3) During the working of the engine, the temperature of the BFJB increases approximately linearly with the increase in the load and the rotational speed. However, compared

with the increase in the rotational speed, the bearing temperature rise caused by the increase in the load is smaller. Therefore, on the basis of the research into the rotor system conducted in this experiment, extended research into other rotor systems can be carried out, and a turbocharger suitable for higher-power engines can be developed.

Author Contributions: Methodology, Y.Z.; validation, L.S. and F.D.; formal analysis, Z.X.; investigation, S.Z.; resources, S.D.; writing—original draft preparation, K.Z. All authors have read and agreed to the published version of the manuscript.

Funding: This work was funded by the Basic Research Program of the National Nature Science Foundation of China, grant number 51775025 and 51775013, China Key Research and Development Plan (No. 2017YFB0102102, 2018YFB0104100).

Institutional Review Board Statement: Not applicable.

Informed Consent Statement: Not applicable.

Data Availability Statement: The data used to support the findings of this study are included within the article.

Conflicts of Interest: The authors declare no conflict of interest.

References

1. Andres, L.S.; Chirathadam, R.A. Measurements of Drag Torque, Lift-Off Journal Speed, and Temperature in a Metal Mesh Foil Bearing. *J. Eng. Gas Turbines Power* **2010**, *132*, 2201–2210.
2. Dellacorte, C.; Pinkus, O. Tribological Limitations in Gas Turbine Engines: A Workshop to Identify the Challenges and Set Future Directions. In Proceedings of the Tribological Limitations in Gas Turbine Engines, Albany, NY, USA, 1 May 2000.
3. Radil, K.; Zeszotek, M. An Experimental Investigation into the Temperature Profile of a Compliant Foil Air Bearing. *Tribol. Trans.* **2004**, *47*, 470–479. [[CrossRef](#)]
4. Agrawal, G.L. Foil Air/Gas Bearing Technology—An Overview. In Proceedings of the International Gas Turbine & Aeroengine Congress & Exhibition, Orlando, FL, USA, 2 June 1997.
5. Weibin, L. *Study of Bump-Type Foil Aero-Dynamic Bearing's Application on an Aero-Engine*; Civil Aviation University of China: Tianjin, China, 2017.
6. Rui, Y. *Study on Rotordynamic Characteristics and Experimental Verification of Rotor System of Oil-Free Turbocharger*; Hunan University: Changsha, China, 2017.
7. Walton, J.F.; Heshmat, H. Application of Foil Bearings to Turbomachinery Including Vertical Operation. *J. Eng. Gas Turbines Power* **2002**, *124*, 1032–1041. [[CrossRef](#)]
8. Shuiting, D.; Yue, S. Analysis on development trend and key technology of aircraft heavy fuel piston engine. *J. Aerosp. Power* **2021**, *36*, 1121–1136.
9. Yu, Z.; Tong, X. Digital-twin-driven geometric optimization of centrifugal impeller with free-form blades for five-axis flank milling. *J. Manuf. Syst.* **2020**, *58*, 22–35.
10. Weisong, X.; Xin, L. Review of Technique Application and performance Evaluation for Aerodynamic Elastic Foil Gas Bearing in Aero-engine. *Lubr. Eng.* **2018**, *43*, 136–147.
11. Yu, Z.; Yue, S. Parametric modeling method for integrated design and manufacturing of radial compressor impeller. *Int. J. Adv. Manuf. Technol.* **2020**, *112*, 1–15.
12. Qi, S.M.; Geng, H.P.; Yu, L. New Method for the Calculation of the Characteristics of Aerodynamic Bearings. *J. Mech. Strength* **2006**, *28*, 369–373.
13. San Andrés, L.; Ryu, K. Thermal management and rotordynamic performance of a hot rotor-gas foil bearings system. Part 1: Measurements. *ASME J. Eng. Gas Turbines Power* **2011**, *133*, 253–262. [[CrossRef](#)]
14. Rudloff, L. Experimental Analyses of a First Generation Foil Bearing: Start-Up Torque and Dynamic Coefficients. *J. Eng. Gas Turbines Power* **2011**, *133*, 92501. [[CrossRef](#)]
15. Radil, K.; Dellacorte, C. Foil Bearing Starting Considerations and Requirements for Rotorcraft Engine Applications. In Proceedings of the 65th Annual Forum Proceedings, Grapevine, TX, USA, 1 August 2009.
16. Rubio, D.; Andrés, L.S. Bump-Type Foil Bearing Structural Stiffness: Experiments and Predictions. *J. Eng. Gas Turbines Power* **2006**, *128*, 653–660. [[CrossRef](#)]
17. Xingjun, S.; Gang, X. Engineering Experimental Investigation on the Performance of Large Load Capacity Air Foil Bearing. *J. Lubrication Eng.* **2017**, *42*, 125–131.
18. Dickman, J.R. *An Investigation of Gas Foil Thrust Bearing Performance and its Influencing Factors*; Case Western Reserve University: Cleveland, OH, USA, 2010.
19. Blok, H.; Rossum, J. The Foil Bearing—A New Departure in Hydrodynamic Lubrication. *Lubr. Eng.* **1953**, *9*, 316–320.

20. Hu, L.; Zhang, G. Performance analysis of multi-leaf oil lubricated foil bearing. *Proc. Inst. Mech. Eng. Part J J. Eng. Tribol.* **2013**, *227*, 962–979. [[CrossRef](#)]
21. Dellacorte, C. A New Foil Air Bearing Test Rig for Use to 700 °C and 70,000 rpm. *Tribol. Trans.* **2008**, *41*, 335–340. [[CrossRef](#)]
22. Braun, M.J.; Choy, F.K. Two-Dimensional Dynamic Simulation of a Continuous Foil Bearing. *Tribol. Int.* **1996**, *29*, 61–68. [[CrossRef](#)]
23. Feng, K.; Deng, Z.; Zhao, X. Test on static and temperature characteristics of gas foil bearing. *J. Aerosp. Power* **2017**, *32*, 1394–1399.
24. Xie, Y.Q. *Design and Experimental Study of an Oil Free Turbocharger*; Hunan University: Changsha, China, 2015; p. 81.
25. Pattanayak, M.R.; Pandey, R.K. Performance behaviours of a self-acting gas journal bearing with a new bore design. *Tribol. Int.* **2020**, *151*, 711–718. [[CrossRef](#)]
26. Ganai, P.; Pandey, R.K. Performance improvement of foil air journal bearing employing micro- pocket and textures on top compliant surface. *Surf. Topogr. Metrol. Prop.* **2021**, *9*, 025045. [[CrossRef](#)]
27. Samanta, P.; Murmu, N.C. The evolution of foil bearing technology. *Tribol. Int.* **2019**, *135*, 305–323. [[CrossRef](#)]
28. Liu, X.; Li, C.; Du, J.; Nan, G. Thermal Characteristics Study of the Bump Foil Thrust Gas Bearing. *Appl. Sci.* **2021**, *11*, 4311. [[CrossRef](#)]
29. Kumar, J.; Khamari, D.S. A review of thermohydrodynamic aspects of gas foil bearings. *Proc. Inst. Mech. Eng. Part J J. Eng. Tribol.* **2021**, 1591214344. [[CrossRef](#)]
30. Salehi, M.; Swanson, E. Thermal Features of Compliant Foil Bearings—Theory and Experiments. *J. Tribol.* **2001**, *123*, 566–571. [[CrossRef](#)]
31. Peng, Z.; Khonsari, M. A Thermohydrodynamic Analysis of Foil Journal Bearings. *J. Tribol.* **2006**, *128*, 534–541. [[CrossRef](#)]
32. Yu, Z.; Lifeng, H. Investigation on transient dynamics of rotor system in air turbine starter based on magnetic reduction gear. *J. Adv. Manuf. Sci. Technol.* **2021**, *1*, 2021009-1–2021009-9.
33. Feng, K.; Kaneko, S. A Thermohydrodynamic Sparse Mesh Model of Bump-Type Foil Bearings. *J. Eng. Gas Turbines Power* **2013**, *135*, 022501. [[CrossRef](#)]
34. Liu, L.j. *Theoretical Considerations of Hydrodynamic and Thermal Characteristics of Gas Foil Thrust Bearings*; Hunan University: Changsha, China, 2015.
35. Andrés, L.S.; Kim, T.H. Thermohydrodynamic Analysis of Bump Type Gas Foil Bearings: A Model Anchored to Test Data. *J. Eng. Gas Turbines Power Trans. ASME* **2010**, *132*, 042504. [[CrossRef](#)]
36. Andrés, L.S.; Kim, T.H. Thermal Management and Rotordynamic Performance of a Hot Rotor-Gas Foil Bearings System: Part 2—Predictions versus Test Data. In Proceedings of the ASME Turbo Expo 2010: Power for Land, Sea, and Air, American Society of Mechanical Engineers, Glasgow, UK, 14–18 June 2010; pp. 263–271.
37. Tianwei, L.; Yu, G. Numerical and Experimental Studies on Stability of Cryogenic Turbo-Expander with Protuberant Foil Gas Bearings. *Cryogenics* **2018**, *96*, 62–74.
38. Xu, C.R. Testing Analysis of the Bump Foil Bearing with MoS₂ Coating. *J. Tribol.* **1988**, *1*, 37–41.
39. Ren, S.Q.; Yang, Y.F. Effect of rotational error of precision centrifugal main axel on working radius. *J. Harbin Inst. Technol.* **2000**, *1*, 54–57.
40. Bonello, P.; Hassan, M. An experimental and theoretical analysis of a foil-air bearing rotor system. *J. Sound Vib.* **2018**, *413*, 395–420. [[CrossRef](#)]
41. Li, C.L.; Du, J.J. Temperature calculation and static and dynamic characteristics analysis of bump foil gas bearing. *J. Harbin Inst. Technol.* **2017**, *49*, 46–52.
42. Hassan, M.B.; Bonello, P. A new modal-based approach for modelling the bump foil structure in the simultaneous solution of foil-air bearing rotor dynamic problems. *J. Sound Vib.* **2017**, *396*, 255–273. [[CrossRef](#)]
43. Zhang, X.B.; Ding, S.T. Investigation on gas lubrication performance of porous gas bearing considering velocity slip boundary condition. *Friction* **2022**, *10*, 891–910. [[CrossRef](#)]
44. Feng, K.; Kaneko, S. A Study of Thermohydrodynamic Features of Multi Wound Foil Bearing Using Lobatto Point Quadrature. *ASME Turbo Expo Power Land Sea Air* **2009**, 43154, 911–922.
45. Sim, K.; Kim, T.H. Thermohydrodynamic analysis of bump-type gas foil bearings using bump thermal contact and inlet flow mixing models. *Tribol. Int.* **2012**, *48*, 137–148. [[CrossRef](#)]
46. Kai, F. Thermal Characteristic Analysis of Novel Three-pad Radial Gas Foil Hydrodynamic Bearings. *J. Hunan Univ. (Nat. Sci.)* **2020**, *47*, 35–44.
47. Maraiy, S.Y.; Crosby, W.A. Thermohydrodynamic analysis of airfoil bearing based on bump foil structure. *Alex. Eng. J.* **2016**, *55*, 2473–2483. [[CrossRef](#)]
48. Lee, D.; Kim, D. Thermohydrodynamic Analyses of Bump Air Foil Bearings with Detailed Thermal Model of Foil Structures and Rotor. *J. Tribol.* **2010**, *132*, 16–22. [[CrossRef](#)]
49. Heshmat, H. Advancements in the Performance of Aerodynamic Foil Journal Bearings: High Speed and Load Capability. *J. Tribol.* **1994**, *116*, 287. [[CrossRef](#)]
50. Zhou, Y.; Shao, L.T. Numerical and experimental investigation on dynamic performance of bump foil journal bearing based on journal orbit. *Chin. J. Aeronaut.* **2021**, *02*, 586–600. [[CrossRef](#)]
51. Zhou, T.; Hu, M. Vibration features of rotor unbalance and rub-impact compound fault. *J. Adv. Manuf. Sci. Technol.* **2022**, *33*, 611–619. [[CrossRef](#)]

-
52. Guo, Z.Y. Effects of static and imbalance loads on nonlinear response of rigid rotor supported on gas foil bearings. *Mech. Syst. Signal Process.* **2018**, *133*, 106271. [[CrossRef](#)]
 53. Liu, J.; Du, F.R. Experiment Study on Lift-Off Speed of Bump Foil Journal Bearings. *Bearing* **2013**, *8*, 27–29.